Title: Macromolecular Design Strategies for Preventing Active-Material Crossover in Non-Aqueous All-Organic Redox-Flow Batteries

Authors: Sean E. Doris; Ashleigh L. Ward; Artem Baskin; Peter D. Frischmann; Nagarjuna Gavvalapalli; Etienne Chenard; Christo Sevov; David Prendergast; Jeffrey S. Moore; Brett A. Helms, PhD

To be cited as: 10.1002/anie.201610582

Link to VoR: https://doi.org/10.1002/anie.201610582

Macromolecular Design Strategies for Preventing Active-Material Crossover in Non-Aqueous All-Organic Redox-Flow Batteries

Sean E. Doris,[a] Ashleigh L. Ward,[b] Artem Baskin,[b] Peter D. Frischmann,[b] Nagarjuna Gavvalapalli,[c] Etienne Chénard,[c] Christo S. Sevov,[d] David Prendergast,[b][e] Jeffrey S. Moore,[c] and Brett A. Helms*[b][e]

Abstract: Intermittent energy sources, including solar and wind, require scalable, low-cost, multi-hour energy storage solutions in order to be effectively incorporated into the grid. All-Organic non-aqueous redox-flow batteries offer a solution, but suffer from rapid capacity fade and low Coulombic efficiency due to the high permeability of redox-active species across the battery's membrane. Here we show that active-species crossover is arrested by scaling the membrane's pore size to molecular dimensions and in turn increasing the size of the active material above the membrane's pore-size exclusion limit. When oligomeric redox-active organics (RAOs) were paired with microporous polymer membranes, the rate of active-material crossover was reduced more than 9,000-fold compared to traditional separators at minimal cost to ionic conductivity. This corresponds to an absolute rate of RAO crossover of less than 3 µmol cm^{-2} day^{-1} (for a 1.0 M concentration gradient), which exceeds performance targets recently set forth by the battery industry. This strategy was generalizable to both high and low-potential RAOs in a variety of non-aqueous electrolytes, highlighting the versatility of macromolecular design in implementing next-generation redox-flow batteries.

All-Organic redox-flow batteries are well positioned to offer low-cost, multi-hour electrochemical energy storage at large scale in line with targets for grid modernization.[1-6] During flow-battery operation, solutions of redox-active organic molecules (ROMs) in a non-aqueous electrolyte are circulated through the negative and positive electrode compartments of an electrochemical cell. These compartments are electronically isolated from each other by a separator or ion-conducting membrane.[7,8] In order to maximize cycle-life and efficiency, it is imperative to block ROMs from migrating between electrode compartments during cycling while also maintaining facile transport of the working ion.[9]

Here we show how this is achieved through macromolecular design principles advanced and applied to ROMs and ion-selective membranes derived from polymers of intrinsic microporosity (PIMs) (Figure 1). In contrast with traditional mesoporous battery separators, membranes derived from PIMs feature permanent micropores that in principle allow working-ion conduction while blocking the crossover of larger active-materials.[10-15] Indeed, we found that the effective diffusion coefficient (D_{eff}) for small-molecule ROMs (e.g., **1a**) through PIM-1 membranes decreased 40-fold compared to a Celgard separator with ~20 nm pores. Additional gains in blocking-ability (470-fold) were obtained by chemically cross-linking PIM-1 membranes, which restricted pore swelling in electrolyte. While these gains alone are impressive, we hypothesized that simply increasing the effective size of the ROM (e.g., through oligomerization) would provide active-materials that were larger than the PIM membrane's pore-size exclusion limit and thereby enable active-material blocking through a size-sieving mechanism. Indeed, by slightly increasing the molecular dimensions from 8.8 to 12.3 Å through oligomerization (Figure 2), D_{eff} fell below our experimental limit of quantification, with an estimated upper-bound of 3.4×10^{-11} cm^2 s^{-1}. Despite this >9,000-fold improvement in membrane blocking ability relative to Celgard, PIM-1 membranes retained high ionic conductivities of at least 0.4 mS cm^{-1} (compared to 2.2 mS cm^{-1} for Celgard). Furthermore, we found that sieving oligomeric organic active materials (RAOs) by size with PIM membranes was general to different ROM chemistries (e.g., **3b** and **3c**) in a variety of battery electrolytes (e.g., ACN, PC, DME, etc.), showcasing the generality of our approach.

Breaking with convention, the advances reported here provide an important counterpoint to: 1) single-component electrodes paired with ceramic membranes, which are expensive and difficult to scale;[16] 2) thick macroporous separators paired with mixed-electrode formulations (i.e., anolytes and catholytes present in both electrode compartments), which lead to Coulombic inefficiencies and short cycle-life;[17,18] and 3) mesoporous separators paired with concentrated solutions of redox-active polymers (RAPs), which are difficult to pump through electrochemical cells at high molecular weight and at all states-of-charge.[19-23] Our strategy to implement RAOs, as opposed to RAPs, should also serve to retain the facile charge transfer kinetics that are characteristic of ROMs, which is essential for power quality and high active-material utilization.[24]

---

[a] S.E. Doris
Department of Chemistry
419 Latimer Hall, University of California, Berkeley
Berkeley, CA 94720, USA
[b] Dr. A.L. Ward, Dr. A. Baskin, Dr. P.D. Frischmann, Dr. D. Prendergast, Dr. B.A. Helms*
Joint Center for Energy Storage Research
Lawrence Berkeley National Laboratory
1 Cyclotron Road, Berkeley, CA 94720, USA
E-mail: bahelms@lbl.gov
[c] Dr. N. Gavvalapalli, Dr. E. Chénard, Prof. J.S. Moore
Joint Center for Energy Storage Research
University of Illinois at Urbana-Champaign
505 South Matthews Avenue
Urbana, IL 61801, USA
[d] Dr. C.S. Sevov
Joint Center for Energy Storage Research
University of Michigan
930 North University Avenue
Ann Arbor, MI 48109, USA
[e] Dr. D. Prendergast, Dr. B.A. Helms*
The Molecular Foundry
Lawrence Berkeley National Laboratory
1 Cyclotron Road, Berkeley, CA 94720, USA

Supporting information for this article is given via a link at the end of the document.

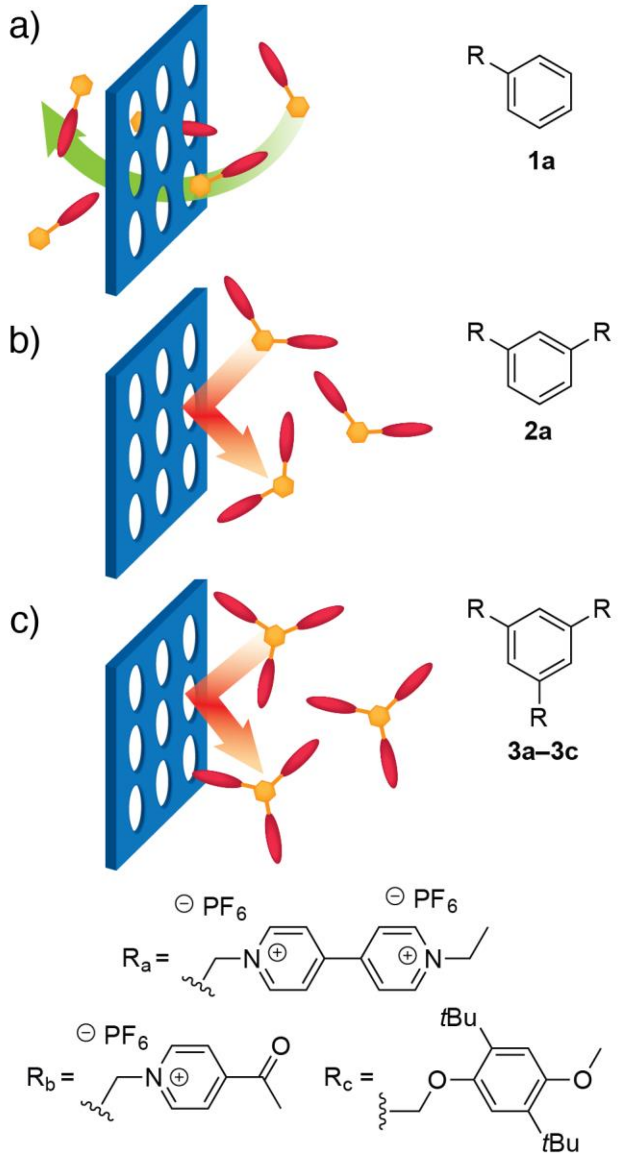

Figure 1. Macromolecular design strategies for preventing active-material crossover in all-organic redox-flow batteries: a) Small-molecule redox-active organic molecules (ROMs) pass through microporous membranes; b) and c) larger redox-active oligomers (RAOs) are blocked from passing through the membrane by a size-sieving mechanism.

To quantitatively inform the critical size regime for ROM-blocking by a size-selective polymer membrane, we designed a series of structurally minimal viologen-based ROMs and RAOs (**1a**–**3a**, Figure 1) and studied their solvated structures computationally in acetonitrile (ACN) using a combination of ab initio quantum mechanical studies and classical molecular dynamics simulations (see SI, Figures S1–S6, Tables S1–2). We were interested in understanding active-material solvation at different states of charge (SOCs), as the solvation will determine the effective size of each molecule and changes in solvation may affect the crossover behavior during cell cycling. For each RAO, we calculated the average number of ACN molecules as a function of distance from the molecule's Van der Waals surface (Figure 2) and found that the RAO solvation shells do not change significantly at different SOCs. This implies that membranes that are blocking to active-materials at one SOC will also block their crossover as the battery is cycled and the SOC changes. Furthermore, ACN molecules and PF_6^- counter-ions in the solvation shell are only weakly associated with the RAOs, and the solvation of RAOs in ACN does not lead to significant changes in conformation with respect to isolated geometries (Figures S5–S6). Therefore, the hydrodynamic radii and associated volumes of RAOs were computed from quantum mechanical calculations of isolated clusters. Characteristic sizes for viologen monomer (**1a**), dimer (**2a**) and trimer (**3a**) were 8.8, 12.3, and 16.8 Å, respectively—suggesting that polymer membranes with pore dimensions below 1.2 nm are likely to block the viologen dimer and trimer while considerably smaller pores would be required to sieve the monomer.

To validate the theoretical predictions of a critical size-regime for ROM-blocking, we synthesized **1a** (84%), **2a** (80%), and **3a** (69%) by a simple displacement reaction involving *N*-ethyl-4,4'-bipyridinium hexafluorophosphate and benzyl bromide, 1,3-bis(bromomethyl)benzene, and 1,3,5-tris(bromomethyl)benzene, respectively. Cyclic voltammetry of each compound showed that **1a**, **2a**, and **3a** are reversibly reduced at –0.75 V *vs.* Ag/Ag^+ (Figure S7, Table S3). This low reduction potential along with the high solubility of each species in ACN is promising for their use as energy dense anolytes in all-organic redox-flow batteries.[1] The crossover behavior for each RAO/membrane pairing was quantified by measuring the effective diffusion coefficient (D_{eff}) of each RAO through different membranes (Figures 3 and S8–9, Tables S4–5, see SI for details). Membrane blocking-ability was quantified by comparing each RAO's diffusion coefficient through the membrane (D_{eff}) to its diffusion coefficient through solution (D_{sol}). For the non-selective Celgard membrane, high values for D_{eff}—$(5.4 \pm 0.4) \times 10^{-7}$, $(3.1 \pm 0.3) \times 10^{-7}$, and $(2.2 \pm 0.2) \times 10^{-7}$ cm^2 s^{-1} for **1a**, **2a**, and **3a**, respectively—were measured. These D_{eff} are only 30-fold lower than D_{sol} for each species, indicating that the blocking-ability of Celgard is equally poor for **1a**, **2a**, and **3a**. PIM-1 membranes, which feature nanometer-sized pores, significantly outperformed Celgard, with **1a**, **2a**, and **3a** diffusing through the membrane 1,280, 11,600, and 32,900-fold slower, respectively, than through solution (Figure 3b). This dramatic improvement in membrane blocking-ability upon reducing the pore size from approximately 20 nm to less than 1 nm, along with the improved membrane blocking-ability for larger RAOs, is indicative of size-selective transport of the active materials. However, our theoretical calculations of the sizes of **2a** and **3a** imply that both should be completely blocked by PIM-1 membranes. We hypothesized that swelling of the PIM-1 membranes in electrolyte increases the average pore size above the 0.9 nm pores present in dry membranes,[25] thus allowing some crossover of the larger RAOs.

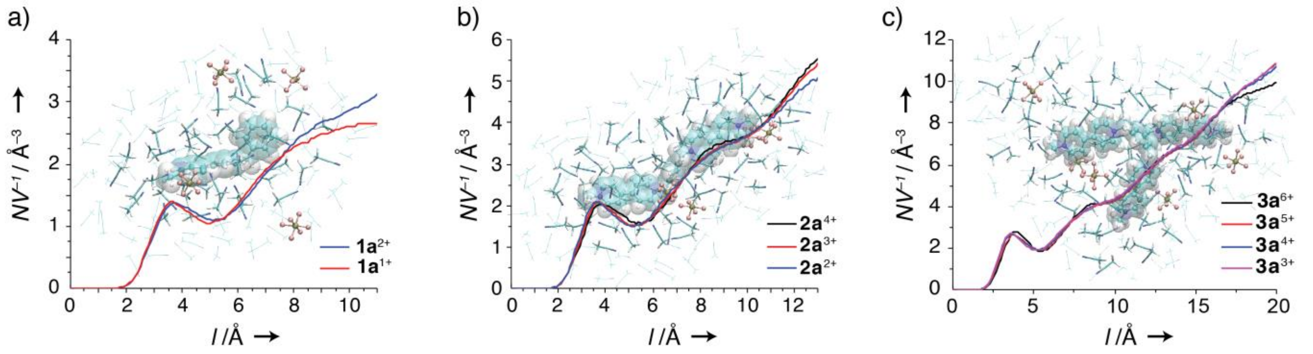

Figure 2. Computed solvation structures of a) **1a**, b) **2a**, and c) **3a** for different SOCs. The density of ACN molecules (NV^{-1}) as a function of distance (l) from each molecule's Van der Waals surface does not vary dramatically at different SOCs. Characteristic sizes of 8.8, 12.3, and 16.8 Å for **1a**, **2a**, and **3a**, respectively, were calculated from quantum mechanical calculations of isolated clusters with similar structures to the solvated clusters.

By cross-linking PIM-1, the degree of swelling is controllable, and the membrane pore size is further constricted. Cross-linking was accomplished by casting solutions of PIM-1 containing the cross-linking agent 2,6-bis(4-azidobenzylidene)-cyclohexanone. Upon heating the membranes, the azide groups of the cross-linking agent are converted to reactive nitrenes, which insert into C–H bonds on the polymer and cross-link the membranes (Figure S10).[11,26] Cross-linked PIM-1 membranes exhibited the best active-species blocking-ability observed by any porous membrane platform to date, with **1a** diffusing through the membrane 14,200-fold slower than through solution, and **2a** and **3a** diffusing slower than the limit of quantification (297,000 and 85,000-fold slower, respectively, than through solution). This unprecedented 9,000-fold improvement in blocking-ability for **2a** (with respect to Celgard) came at minimal cost to ionic conductivity, with cross-linked PIM-1 membranes only 5-fold less conductive than Celgard (0.4 *vs.* 2.2 mS cm^{-1}, Figures S11–12).

To demonstrate that oligomerization is a generalizable approach to blocking ROM crossover in all-organic non-aqueous redox-flow batteries, we synthesized trimeric RAOs based on acylpyridinium hexafluorophosphate (**3b**, 89%) and DB3 (**3c**, 90%) redox-active pendant groups. Monomeric forms of these RAOs have been identified as promising candidates for non-aqueous redox-flow batteries, although their crossover through the battery membrane remains an issue.[2,3,27] Consistent with these reports, cyclic voltammetry showed evidence for reversible reduction of **3b** at –1.40 V *vs.* Ag/Ag$^+$ in 0.1 M TBAPF$_6$/propylene carbonate (PC). Likewise, **3c** underwent reversible oxidation at 0.56 V *vs.* Ag/Ag$^+$ in 0.1 M TBAPF$_6$/dimethoxyethane (DME). Both **3b** and **3c** were blocked by cross-linked PIM-1 membranes, with **3b** diffusing through the membrane slower than the lower limit of quantification of 1.0 × 10^{-11} cm^2 s^{-1} and **3c** diffusing through the membrane with D_{eff} = (8.1 ± 0.7) × 10^{-10} cm^2 s^{-1} (Figure 4). This corresponds to 26,000 and 460-fold improvements in the crossover rate of **3b** and **3c**, respectively, when compared to their diffusion through non-selective mesoporous separators. Clearly, oligomerization provides a straightforward path to preparing a wide variety of RAOs that are effectively blocked by microporous polymer membranes.

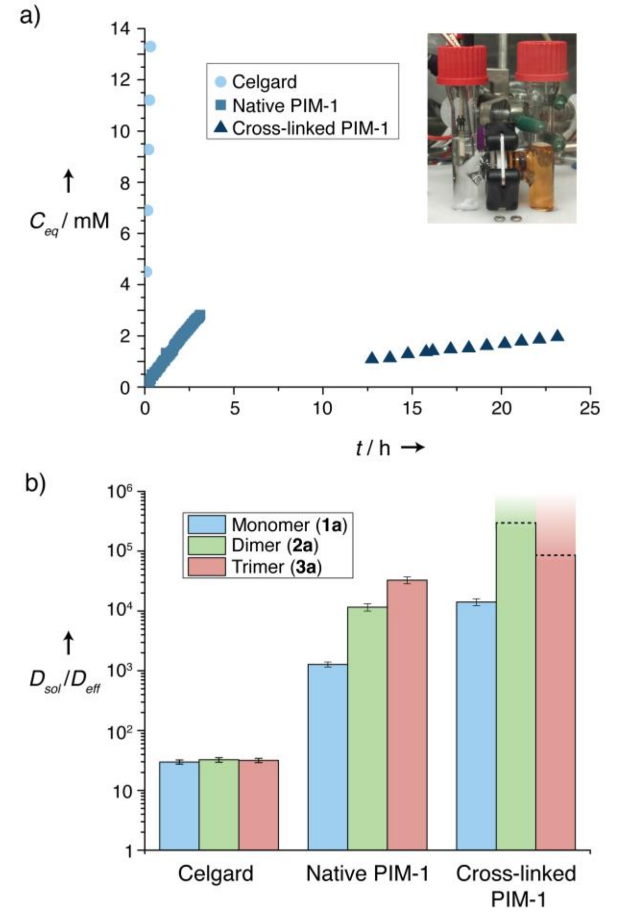

Figure 3. a) Equivalent concentration (C_{eq}) of **1a** in the permeate compartment as a function of time (t) for Celgard, native PIM-1, and cross-linked PIM-1 membranes. (inset) Picture of the crossover cell used to measure D_{eff}, b) Membrane blocking ability for each membrane paired with **1a**–**3a**. D_{sol}/D_{eff} describes how much slower the molecule diffuses through the membrane than through solution. The diffusion of **2a** and **3a** through cross-linked PIM-1 membranes was slower than the lower limit of quantification, so the minimum possible value of D_{sol}/D_{eff} is indicated by dashed lines.

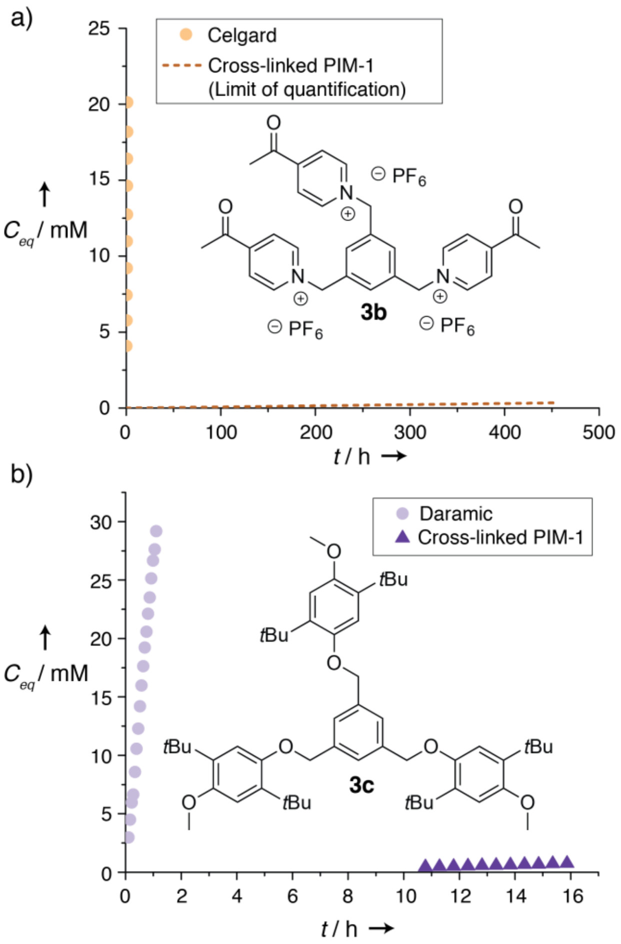

Figure 4. Equivalent RAO concentration (C_{eq}) in the permeate compartment as a function of time (t) for a) **3b** and b) **3c** paired with non-selective mesoporous and cross-linked PIM-1 membranes. The concentration of **3b** never reached the lower limit of quantification when paired with cross-linked PIM-1 (indicated by a dashed line), which is indicative of a size-sieving mechanism.

Macromolecular design of both membranes and active-species is a powerful approach for solving the crossover problem in all-organic redox-flow batteries. Here we showed how computational chemistry informs the design of ROM oligomers, or RAOs, and that by pairing RAOs with RAO-blocking microporous PIM membranes, active-material crossover is reduced by nearly four orders of magnitude with respect to commercially available battery separators with negligible decreases in ionic conductivity. ROM oligomerization was demonstrated for several redox-active motifs, including those that serve as either negative or positive electrode materials in redox-flow batteries. In all cases, RAO crossover was effectively blocked in a variety of battery solvents, including ACN, PC, and DME. These promising results point the way forward towards the design of new classes of RAOs and membranes for all-organic redox-flow batteries, along with their incorporation in next-generation redox-flow battery prototypes.

Experimental Section

Materials and methods, synthetic details, characterization, and membrane preparation are all described in the Supporting Information. All membranes were soaked in electrolyte (0.1 M $LiPF_6$ in ACN for **1a–3a**, 0.1 M $TBAPF_6$ in PC for **3b**, or 0.1 M $TBAPF_6$ in DME for **3c**) for at least 12 h before use. To allow comparison of membranes with different thicknesses, equivalent concentration (C_{eq}) refers to the concentration of ROM or RAO that would be observed with a 10 µm membrane and C_0 = 0.1 M (raw data can be found in the Supporting Information).

Acknowledgements

We thank C. Li and L. Maserati for samples of PIM-1. We thank D. Loudermilk from the UIUC School of Chemical Sciences Graphic Services Facility for assistance in the preparation of Fig. 1. A.L.W., A.B., P.D.F., N.G., E.C., C.S.S., D.P., J.S.M., and B.A.H. were supported by the Joint Center for Energy Storage Research, an Energy Innovation Hub funded by the U.S. Department of Energy, Office of Science, Office of Basic Energy Sciences. S.E.D. was supported by the Department of Defense through the National Defense Science and Engineering Graduate Fellowship program. Portions of this work, including polymer synthesis and characterization, crossover measurements, and electrochemical experiments were carried out as user projects at the Molecular Foundry, which is supported by the Office of Science, Office of Basic Energy Sciences of the U.S. Department of Energy under contract no. DE-AC02-05CH11231. The computational portion of this work was supported by a user project at the Molecular Foundry and its computer cluster (Vulcan), managed by the High Performance Computing Services Group at Lawrence Berkeley National Laboratory (LBNL), and by the computing resources of the National Energy Research Scientific Computing Center, LBNL, both of which are supported by the Office of Science of the U.S. Department of Energy under the same contract.

Keywords: Energy Storage • Macromolecular Chemistry • Membranes • Polymers • Redox-Flow Batteries

[1] R. M. Darling, K. G. Gallagher, J. A. Kowalski, S. Ha, F. R. Brushett, *Energy Environ. Sci.* **2014**, *7*, 3459.

[2] F. R. Brushett, J. T. Vaughey, A. N. Jansen, *Adv. Energy Mater.* **2012**, *2*, 1390.

[3] C. S. Sevov, R. E. M. Brooner, E. Chénard, R. S. Assary, J. S. Moore, J. Rodríguez-López, M. S. Sanford, *J. Am. Chem. Soc.* **2015**, *137*, 14465.

[4] B. Dunn, H. Kamath, J.-M. Tarascon, *Science* **2011**, *334*, 928.

[5] W. Wang, Q. Luo, B. Li, X. Wei, L. Li, Z. Yang, *Adv. Funct. Mater.* **2013**, *23*, 970.

[6] J. Noack, N. Roznyatovskaya, T. Herr, P. Fischer, *Angew. Chem. Int. Ed.* **2015**, *54*, 9776; *Angew. Chem.* **2015**, *127*, 9912.

[7] P. Arora, Z. Zhang, *Chem. Rev.* **2004**, *104*, 4419.

[8] S.-H. Shin, S.-H. Yun, S.-H. Moon, *RSC Adv.* **2013**, *3*, 9095.

[9] R. M. Darling, K. G. Gallagher, W. Xie, L. Su, F. R. Brushett, *J. Electrochem. Soc.* **2016**, *163*, A5029.

[10] C. Li, A. L. Ward, S. E. Doris, T. A. Pascal, D. Prendergast, B. A. Helms, *Nano Lett.* **2015**, *15*, 5724.

[11] S. E. Doris, A. L. Ward, P. D. Frischmann, L. Li, B. A. Helms, *J. Mater. Chem. A* **2016**, *4*, 16946.

[12] N. B. McKeown, P. M. Budd, *Chem. Soc. Rev.* **2006**, *35*, 675.

[13] P. M. Budd, B. S. Ghanem, S. Makhseed, N. B. McKeown, K. J. Msayib, C. E. Tattershall, *Chem. Commun.* **2004**, , 230.

[14] N. B. McKeown, P. M. Budd, *Macromolecules* **2010**, *43*, 5163.

[15] P. Marchetti, M. F. J. Solomon, G. Szekely, A. G. Livingston, *Chem. Rev.* **2014**, *114*, 10735.

[16] P. Knauth, *Solid State Ionics* **2009**, *180*, 911.

[17] W. Duan, R. S. Vemuri, J. D. Milshtein, S. Laramie, R. D. Dmello, J. Huang, L. Zhang, D. Hu, M. Vijayakumar, W. Wang, J. Liu, R. M. Darling, L. Thompson, K. Smith, J. S. Moore, F. R. Brushett, X. Wei, *J. Mater. Chem. A* **2016**, *4*, 5448.

[18] X. Wei, W. Xu, J. Huang, L. Zhang, E. Walter, C. Lawrence, M. Vijayakumar, W. A. Henderson, T. Liu, L. Cosimbescu, B. Li, V. Sprenkle, W. Wang, *Angew. Chem. Int. Ed.* **2015**, *54*, 8684; *Angew. Chem.* **2015**, *127*, 8808.

[19] G. Nagarjuna, J. Hui, K. J. Cheng, T. Lichtenstein, M. Shen, J. S. Moore, J. Rodríguez-López, *J. Am. Chem. Soc.* **2014**, *136*, 16309.

[20] M. Burgess, J. S. Moore, J. Rodríguez-López, *Acc. Chem. Res.* **2016**, *49*, 2649.

[21] E. C. Montoto, G. Nagarjuna, J. Hui, M. Burgess, N. M. Sekerak, K. Hernández-Burgos, T.-S. Wei, M. Kneer, J. Grolman, K. J. Cheng, J. A. Lewis, J. S. Moore, J. Rodríguez-López, *J. Am. Chem. Soc.* **2016**, *138*, 13230.

[22] T. Janoschka, N. Martin, U. Martin, C. Friebe, S. Morgenstern, H. Hiller, M. D. Hager, U. S. Schubert, *Nature* **2015**, *527*, 78.

[23] J. Winsberg, T. Hagemann, S. Muench, C. Friebe, B. Häupler, T. Janoschka, S. Morgenstern, M. D. Hager, U. S. Schubert, *Chem. Mater.* **2016**, *28*, 3401.

[24] M. Burgess, E. Chénard, K. Hernandez-Burgos, G. Nagarjuna, R. S. Assary, J. Hui, J. S. Moore, J. Rodríguez-López, *Chem. Mater.* **2016**, *28*, 7362.

[25] C. L. Staiger, S. J. Pas, A. J. Hill, C. J. Cornelius, *Chem. Mater.* **2008**, *20*, 2606.

[26] N. Du, M. M. Dal-Cin, I. Pinnau, A. Nicalek, G. P. Robertson, M. D. Guiver, *Macromol. Rapid Commun.* **2011**, *32*, 631.

[27] J. Huang, L. Cheng, R. S. Assary, P. Wang, Z. Xue, A. K. Burrell, L. A. Curtiss, L. Zhang, *Adv. Energy Mater.* **2015**, *5*, 1401782.

Entry for the Table of Contents

COMMUNICATION

Better Sieving Through Chemistry: Macromolecular chemistry provides a general approach for blocking redox-active organic molecules (ROMs) from crossing through battery membranes at minimal cost to ionic conductivity. This advance solves a critical challenge facing next-generation redox-flow batteries, clearing the way toward efficient, low-cost grid-scale energy storage.

*S.E. Doris, A.L. Ward, A. Baskin, P.D. Frischmann, N. Gavvalapalli, E. Chénard, C.S. Sevov, D. Prendergast, J.S. Moore, B.A. Helms**

Page No. – Page No.

Macromolecular Design Strategies for Preventing Active-Material Crossover in Non-Aqueous All-Organic Redox Flow Batteries

Table of Contents

Materials and methods

Materials

4-Acetylpyridine, ammonium hexafluorophosphate, 4,4-bipyridine, 2,5-di-*tert*-butyl-4-methoxyphenol, bromomethylbenzene, 1,3-bis(bromomethyl)benzene, 1,3,5-tris(bromomethyl)benzene, chloroform-d_3 (99.5% atom D), 18-crown-6, 1,2-dimethoxyethane (DME, 99.5%, anhydrous), ethyl iodide, potassium carbonate, propylene carbonate (PC, 99.7%, anhydrous), silver(I) hexafluorophosphate (99.99% trace metals grade), tetrabutylammonium hexafluorophosphate ($TBAPF_6$, 99.0%), tetrafluoroterephthalonitrile (99%), and 3,3,3',3'-tetramethyl-1,1'-spirobisindane-5,5',6,6'-tetraol (96%) were obtained from Sigma-Aldrich. Battery grade lithium hexafluorophosphate ($LiPF_6$) (99.9+%) was obtained from STREM Chemicals, Inc. 2,6-Bis(4-azidobenzylidene)cyclohexanone (90%, wetted with ca. 30% water) was obtained from TCI. *N*-ethyl-4,4'-bipyridinium hexafluorophosphate and viologen monomer (**1a**) were synthesized using reported protocols.[1] Glassy carbon electrodes with 1 mm diameter were purchased from BAS Inc. (West Lafayette, IN) and polished before each experiment with 3-μm diamond paste. Ag/Ag^+ reference electrodes were purchased from CHI instruments (Austin, TX) and filled with 10 mM silver(I) hexafluorophosphate in 0.5 M $LiPF_6$ in ACN (for experiments in ACN) or 0.1 M $TBAPF_6$ in PC or DME (for experiments in PC or DME, respectively). A bulk electrolysis cell with a reticulated vitreous carbon working electrode and platinum wire counter electrode was purchased from BAS Inc. (West Lafayette, IN). Celgard® 2325 was purchased from Celgard (Charlotte, NC). Daramic 175 was received as a free sample from Daramic (Charlotte, NC). *N,N*-dimethylformamide (DMF) and acetonitrile (ACN) were taken from a JC Meyer solvent system. Chloroform (HPLC grade) and methanol were obtained from EMD Millipore. All chemicals were used as received unless otherwise specified. Lithium hexafluorophosphate and tetrabutylammonium hexafluorophosphate were dried under vacuum for 16 h at 100 ˚C and 90 ˚C, respectively. ACN was dried over 3 Å molecular sieves to < 20 ppm water. For experiments with ROM and RAOs **1a**–**3a**, electrolyte refers to 0.1 M $LiPF_6$ in acetonitrile. For experiments with RAOs **3b** or **3c**, electrolyte refers to 0.1 M tetrabutylammonium hexafluorophosphate in propylene carbonate or 1,2-dimethoxyethane, respectively.

Instrumentation

Unless otherwise mentioned, all manipulations were performed in an argon glovebox with oxygen and water levels below 5 and 1 ppm, respectively. ^1H and ^{13}C NMR spectra were recorded on Bruker Avance II 500 MHz, Varian Unity 500, and VXR 500 NMR spectrometers. Chemical shifts are reported in δ (ppm) relative to the residual solvent peak (CD_3CN: 1.94 for ^1H; 1.32 for ^{13}C, $CDCl_3$: 7.24 for ^1H; 77.23 for ^{13}C, DMSO-d_6: 2.50 for ^1H; 39.51 for ^{13}C). Coupling constants (J) are expressed in Hertz (Hz). Splitting patterns are designated as s(singlet), d(doublet), t(triplet), q(quartet), dd(doublet of doublets), and m(multiplet). Low- and high-resolution EI mass spectra were recorded on a Micromass 70-VSE spectrometer. Low- and high-resolution ESI mass spectra were recorded on a Synapt G2 Q-Tof spectrometer. High-resolution ESI-MS of **3b** and **3c** were performed by the University of California, Berkeley QB3/Chemistry Mass Spectrometry Facility. Elemental analyses were performed by the University of California, Berkeley

College of Chemistry Microanalytical Facility. Polymer molecular weight was measured using size-exclusion chromatography with a Malvern Viscotek TDA 302 system calibrated with a 99-kDa monodisperse polystyrene standard. Electrochemical experiments were performed on a Bio-Logic VMP3 potentiostat. Cyclic voltammograms were acquired with iR drop compensation by measuring the uncompensated resistance with a 100 kHz impedance measurement and correcting for 85% of the expected drop. FT-IR spectra were acquired in transmission mode on a Varian 3100 FT-IR spectrometer. Water content measurements were performed on a Mettler Toledo C20 Coulometric KF Titrator Karl-Fischer apparatus.

Synthesis of *N*-ethyl-4,4'-bipyridinium hexafluorophosphate

N-ethyl-4,4'-bipyridinium hexafluorophosphate was synthesized as described previously.[1] Briefly, ethyl iodide (5.12 mL, 64.0 mmol, 1.0 equiv) was added to a solution of 4,4-bipyridine (10.0 g, 64.0 mmol, 1.0 equiv) in DCM (50 mL). As the reaction progressed, an orange solid precipitated from solution. The mixture was stirred for 24 h at RT, and additional orange solid was precipitated from solution by adding diethyl ether. The solid was isolated by filtration and rinsed with DCM/ether (1:1 *v*/*v*). The solid was then dissolved in a minimum volume of water and ammonium hexafluorophosphate (53.0 g, 325 mmol, 5.0 equiv) was added portion-wise. As ammonium hexafluorophosphate was added, a beige solid precipitated out of solution. The resulting mixture was stirred for 24 h, and the solid was isolated by filtration, followed by rinsing with water, methanol, and ether. The resulting solid was dried under vacuum for 24 h to yield *N*-ethyl-4,4'-bipyridinium hexafluorophosphate (6.27 g, 30% yield, 2 steps) as a beige solid.

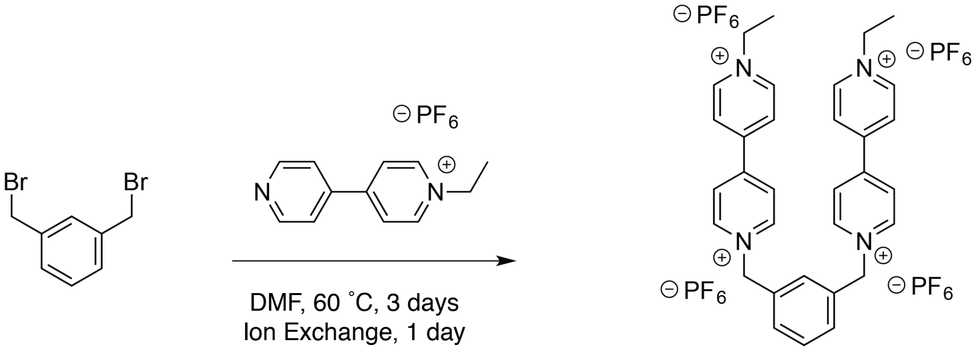

2a

Synthesis of viologen dimer (2a)

1,3-Bis(bromomethyl)benzene (2.5 g, 9.47 mmol, 1.0 equiv) was reacted with *N*-Ethyl-4,4'-bipyridinium hexafluorophosphate (12.5 g, 37.9 mmol, 4 equiv) in DMF. The solution was then allowed to reach 60 °C and stirred at this temperature for 3 days. Solids precipitated out as the reaction progressed. The mixture was added to diethyl ether, and the solids filtered and rinsed with additional diethyl ether. The solids were then dissolved in a minimal amount of acetonitrile/water (1:4, *v/v*) and ammonium hexafluorophosphate

(10 equiv) in a minimal amount of water was added portion wise. The resulting mixture was stirred for 24 h. Acetonitrile was removed under reduced pressure and water was added to the mixture to further precipitate out the solid. The solid was filtered out and rinsed with water, methanol, and diethyl ether. The product was dried under vacuum for 24 h to yield the viologen dimer, **2a** (8.0 g, 80%, 2 steps) as a white powder. ^{1}H NMR (500 MHz, CD_3CN): δ 8.96 – 8.91 (m, 8H), 8.41 – 8.38 (m, 8H), 7.61 – 7.60 (m, 4H), 5.84 (s, 4H), 4.68 (q, *J* = 7.5 Hz, 4H), 1.65 ppm (t, *J* = 5 Hz, 6H); ^{13}C NMR (125 MHz, CD_3CN): δ 151.7, 150.9, 146.8, 146.5 (t, *J* = 8.1 Hz), 146.4, 134.9, 131.9, 131.8, 131.5, 128.5, 128.3, 65.2, 58.8, 16.6 ppm; HRMS (ESI-TOF): *m/z* for $C_{32}H_{34}F_{18}N_4P_3$ $(M-PF_6^-)^+$ calculated 909.1709, found 909.1667.

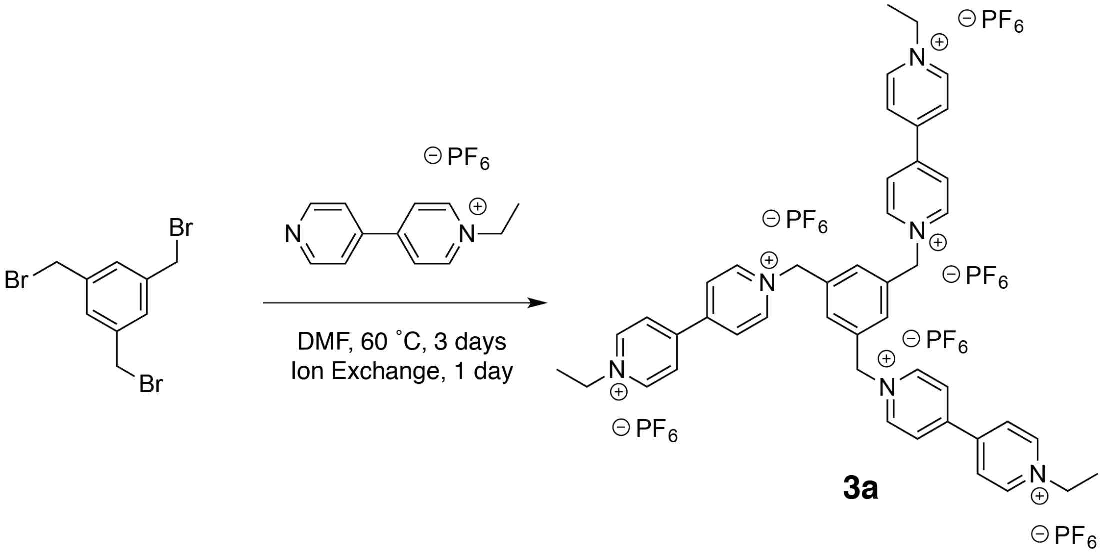

Synthesis of viologen trimer (3a)

1,3,5-Tris(bromomethyl)benzene (3.37 g, 9.46 mmol, 1.0 equiv) was reacted with *N*-ethyl-4,4’-bipyridinium hexafluorophosphate (10.0 g, 30.28 mmol, 3.2 equiv) in DMF. The solution was then allowed to reach 60 °C and stirred at this temperature for 3 days. Solid precipitated out as the reaction progressed. The mixture was added to diethyl ether, and the solid was filtered out and rinsed with additional diethyl ether. The solid was then dissolved in a minimal amount of acetonitrile/water (1:4, *v/v*) and ammonium hexafluorophosphate (10 equiv) in a minimal amount of water was added portion wise. The resulting mixture was stirred for 24 h. Acetonitrile was removed under reduced pressure and water was added to the mixture to further precipitate out the solid. The solid was filtered out and rinsed with water, methanol, and diethyl ether. The solid was dried under vacuum for 24 h to yield the viologen trimer, **3a** (10.3 g, 69%, 2 steps) as a white powder. ^{1}H NMR (500 MHz, CD_3CN): δ 8.92 (d, *J* = 10 Hz, 12H), 8.41 – 8.37 (m, 12H), 7.67 (s, 3H), 5.84 (s, 6H), 4.68 (q, *J* = 7.5 Hz, 6H), 1.65 ppm (t, *J* = 7.5 Hz, 9H); $^{13}C\{^1H\}$ NMR (125 MHz, CD_3CN): δ 152.0, 151.0, 147.0, 146.6, 136.2, 133.1, 128.7, 128.4, 64.9, 59.0, 16.8 ppm; HRMS (ESI): *m/z* for $C_{45}H_{48}N_6PF_6^{5+}$ $(M - 5PF_6^-)^{5+}$ calculated 163.4711, found 163.4710; *m/z* for $C_{45}H_{48}N_6P_2F_{12}^{4+}$ $(M - 4PF_6^-)^{4+}$ calculated 240.5801, found 240.5798; *m/z* for $C_{45}H_{48}N_6P_3F_{18}^{3+}$ $(M - 3PF_6^-)^{3+}$ calculated 369.0950, found 369.0945; Anal. Calc'd for $C_{45}H_{48}N_6P_6F_{36}$: C, 35.04; H, 3.14; N, 5.45; Found: C, 34.92; H, 3.21; N, 5.34.

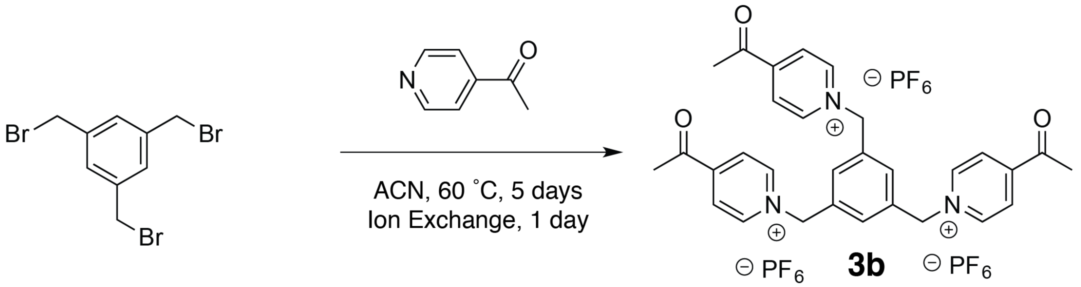

Synthesis of acylpyridinium trimer (3b)

4-Acetylpyridine (10.0 g, 83 mmol, 4.0 equiv) was added to a solution of 1,3,5-tris(bromomethyl)benzene (7.4 g, 21 mmol, 1.0 equiv) in acetonitrile (100 mL). The solution was stirred at 60 °C for 5 days. A precipitate formed, and was filtered and rinsed with diethyl ether. The solid was then dissolved in acetonitrile and water, and ammonium hexafluorophosphate (21.0 g, 130 mmol, 6.2 equiv) was added. The mixture was stirred overnight. Acetonitrile was removed under reduced pressure, and the solid was filtered off, dissolved in a minimal amount of acetonitrile, and precipitated by adding excess water with vigorous stirring. This process was repeated once more, followed by rinsing the solid with methanol (2×) and diethyl ether. The product was dried overnight to yield 17 g of the acylpyridinium trimer, **3b** (89%, over 2 steps). Further purification of **3b** was carried out by dissolving the crude mixture in a minimal amount of acetonitrile and then filtering away the dark-colored solids. Water was added to the filtrate and the mixture was cooled at 4 ˚C to precipitate **3b** as a tan solid, which was isolated by filtration. The product was washed with methanol (50 mL) and diethyl ether (50 mL) before drying in vacuo. ^1H NMR (500 MHz, DMSO-d_6): δ 9.28 (d, *J* = 7 Hz, 6H), 8.55 (d, *J* = 7 Hz, 6H), 7.62 (s, 3H), 5.90 (s, 6H), 2.76 (s, 9H) ppm; $^{13}C\{^1H\}$ NMR (125 MHz, DMSO-d_6): δ 160.6, 149.0, 146.6, 135.8, 126.4, 62.8, 27.4 ppm; HRMS (ESI): *m/z* for $C_{30}H_{30}O_3N_3^{3+}$ $(M - 3PF_6^-)^{3+}$ calculated 160.0757, found 160.0755; *m/z* for $C_{30}H_{30}O_3N_3PF_6^{2+}$ $(M - 2PF_6^-)^{2+}$ calculated 312.5959, found 312.5955; *m/z* for $C_{30}H_{30}O_3N_3P_2F_{12}^{+}$ $(M - PF_6^-)^{+}$ calculated 770.1565, found 770.1554; Anal. Calc'd for $C_{30}H_{30}P_3F_{18}N_3O_3$: C, 39.36; H, 3.30; N, 4.59; Found: C, 39.23; H, 3.48; N, 4.49.

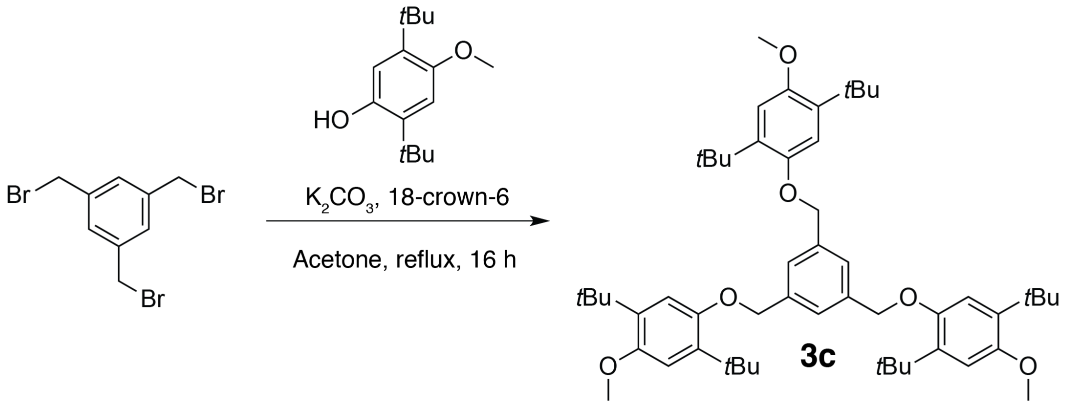

Synthesis of DB3 trimer (3c)

To a solution of 2,5-di-*tert*-butyl-4-methoxyphenol (7.80 g, 33 mmol), 1,3,5-tris(bromomethyl)benzene (3.57 g, 10 mmol), and 18-crown-6 (871 mg, 1.0 mmol) in acetone (50 mL) was added freshly pulverized, oven-dried potassium carbonate (6.83 g, 49.5 mmol) while stirring vigorously. The reaction mixture was heated at reflux for 16 h, cooled, and then the solids filtered; the solids were then washed with dichloromethane (3 × 50 mL). The filtrate was concentrated in vacuo. The crude product was dissolved in diethyl ether (150 mL), which was then extracted with aqueous sodium hydroxide (15% *w/w*) (3 × 50 mL), water (1 × 50 mL), and brine (1 × 50 mL). The ethereal layer was dried over magnesium sulfate, which was removed by filtration. After concentrating the ethereal layer in vacuo, the product was recrystallized from ethanol/dichloromethane to yield **3c** as colorless needles (7.44 g, 90%). ^{1}H NMR (500 MHz, $CDCl_3$): δ 7.52 (s, 3H), 6.89 (s, 3H), 6.85 (s, 3H), 5.10 (s, 6H), 3.81 (s, 9H), 1.37 (s, 27H), 1.32 (s, 27H) ppm; $^{13}C\{^1H\}$ NMR (125 MHz, $CDCl_3$): δ 152.4, 151.3, 138.9, 136.8, 136.5, 125.8, 113.1, 111.9, 71.4, 56.1, 34.9, 34.8, 30.2, 30.0 ppm; HRMS (ESI): *m/z* for $C_{54}H_{78}O_6^+$ $(M)^+$ calculated 822.5793, found 822.5792; Anal. Calc'd for $C_{54}H_{78}O_6$: C, 78.79; H, 9.55; Found: C, 78.81; H, 9.60.

Synthesis of PIM-1

PIM-1 with molecular weight M_W = 386 kg mol^{-1} (M_N = 136 kg mol^{-1}, PDI= 2.8) was synthesized as described elsewhere.[2-4] Briefly, a mixture of anhydrous potassium carbonate (8.3 g, 60 mmol), 3,3,3′,3′-tetramethyl-1,1'-spirobisindane-5,5′,6,6′-tetrol (6.8 g, 20 mmol) and 2,3,5,6-tetrafluoroterephthalonitrile (4.0 g, 20 mmol) in dry DMF was stirred at 65 °C for 4 d. On cooling, the mixture was added to water and the crude product collected by filtration. Repeated precipitations from a concentrated solution of polymer in chloroform into methanol yielded 8.90 g (19.3 mmol, 97% yield) of the fluorescent yellow polymer (PIM-1).

Membrane preparation

PIM-1 was dissolved in chloroform at a concentration of 12.5 mg mL^{-1}. PIM-1 membranes were cast by depositing 1 mL of solution into 3.5 cm diameter Teflon wells. The solvent was left to evaporate under an evaporation dish under ambient pressure for 5 h or until dryness. The films were further dried in vacuo overnight. Cross-linked PIM-1 membranes were prepared by adding 0.1 molar equivalents of 2,6-bis(4-azidobenzylidene)-cyclohexanone to the casting solution. Once dried, the cross-linked films were activated by heating in a vacuum oven at 175 °C for 7.5 h. The dried films were used as cast and Celgard® 2325 membranes were punched into 1 and 3/16 inch circles. All membranes were soaked in electrolyte overnight before use.

Computational methods

Computational methodology

The systematic study of solvation structures of ROMs at different states of charges was performed in two steps. In the first step, the quantum mechanical study of small molecular clusters (isolated molecules) of RAOs (**1a**, **2a**, **3a**), ACN and PF_6^- at T=0 K was carried out. First, we calculated the lowest energy molecular configurations of the RAOs with and without counter-ions and solvent (ACN) molecules. Next we evaluated charge distributions, and performed HOMO/LUMO orbital analysis (Figures S1–3). The purpose of these calculations was to see the distribution of charge in different states of charge as well as to check if there was a significant orbital overlap between viologens, solvent (ACN) molecules and counter-ions (PF_6^-). The effects of finite temperature and condensed liquid phase on the ROMs solvation in ACN were accounted for by the use of classical MD. The Generalized Amber force field[5] (GAFF) was used for solute and solvent molecules as well as for counter-ions. Note that GAFF charges on nitrogen atoms underestimate the effects of the polarity of the ROM molecules. The comparison between the GAFF charge scheme and the charges obtained *ab initio* is shown in Tables S1–S2. Therefore, in our simulations we used GAFF force field parameters in combination with Mulliken partial charges derived from *ab initio* calculations for the optimized geometry of ROMs. The free energy profiles were computed using the metadynamics technique.[6,7] For the study of solvated structures of RAOs/ACN we calculated pair radial distribution functions (rdf) obtained with an algorithm adapted for non-spherical objects. Instead of taking the center of the mass of the ROM molecule as a reference point for the rdf, the algorithm explicitly evaluates the distribution of distances from each atom of the ROM molecule to the solvent molecules (either the center of the mass of ACN or a particular atom in the solvent molecule, e.g., N) by sampling the MD trajectory.

Quantum chemistry calculations

Optimized geometries, relative energies, and molecular orbitals were calculated with the DFT TeraChem package.[8] As suggested in the previous extensive computational studies of aprotic ionic liquids, for RAOs/ACN systems in our calculations we used the B3LYP5-D3 functional with the 6-311++G** basis set[9] employing the third version of Grimme's empirical dispersion correction.[10] We used the L-BFGS geometry optimization method[11] with the termination criterion for the maximum energy gradient component of 4.5×10^{-4} au. The wave function convergence threshold was set as 3.0×10^{-5}. The two-electron integral threshold was set as 1.0×10^{-12}, and the basis set linear dependency threshold was 1.0×10^{-4}. Partial charges were computed using the full natural bond orbital (NBO) and Mulliken analysis. For the open shell molecules unrestricted Kohn-Sham orbitals were computed.

Molecular dynamics calculations

Classical molecular dynamics (MD) simulations were conducted on the solutions (ROMs and RAOs in ACN)—with PF_6^- ions added accordingly to attain zero total charge—using the LAMMPS simulation package.[12] Long-range electrostatic interactions were treated within the particle-mesh Ewald (PME) method with a cutoff distance 1.0 nm with grid spacing in *k*-space of 10^{-5}. A cut-off of 1.0 nm with a spline from 0.9 to 1.0 nm was used for Lennard-Jones interactions. The relaxation of the initial structures was performed in two steps, first using steepest descent with a convergence criterion of 10^{-4} kcal mol^{-1} for energies and 10^{-4} kcal mol^{-1} Å^{-1} for forces. The systems were first heated to 298 K in the canonical ensemble (NVT). To remove any "memory" effects, the systems were first melted at 400 K and then annealed back to 298 K three times (evolving the trajectory 2 ns for annealing each step). Then, isothermal-isobaric (NPT, P=1 atm, T=298 K) simulations were performed for 2 ns (2 fs time step) to obtain the correct density using a Nose/Hoover thermostat and Nose/Hoover barostat.[13,14] Afterwards, NVT simulations were performed (T=298 K) for 1 ns (2 fs time step) to equilibrate and sample the properties of interest. Structural properties were obtained from 10 ns MD simulation runs with an integration time step 1 fs in NVT ensemble. We ran several parallel simulations of solvated **1a**, **2a** and **3a** at different concentrations. For **1a**, C_{ROM}=0.03–0.1 M with a simulation cell (box) size of 4×4×4 nm. For **2a**, C_{ROM}=0.02–0.1 M with a box size of 6×6×6 nm. For **3a**, C_{ROM}=0.01–0.05 M with a box size of 8×8×8 nm.

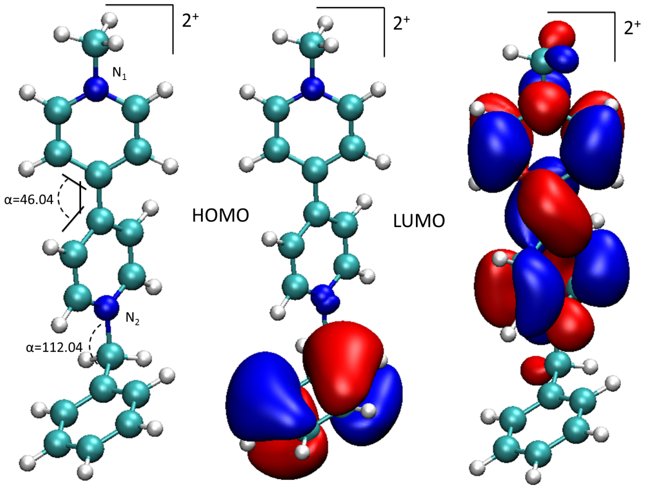

Figure S1. Viologen ROM (**1a**) at 2+ state of charge and optimal configurations of its HOMO and LUMO orbitals.

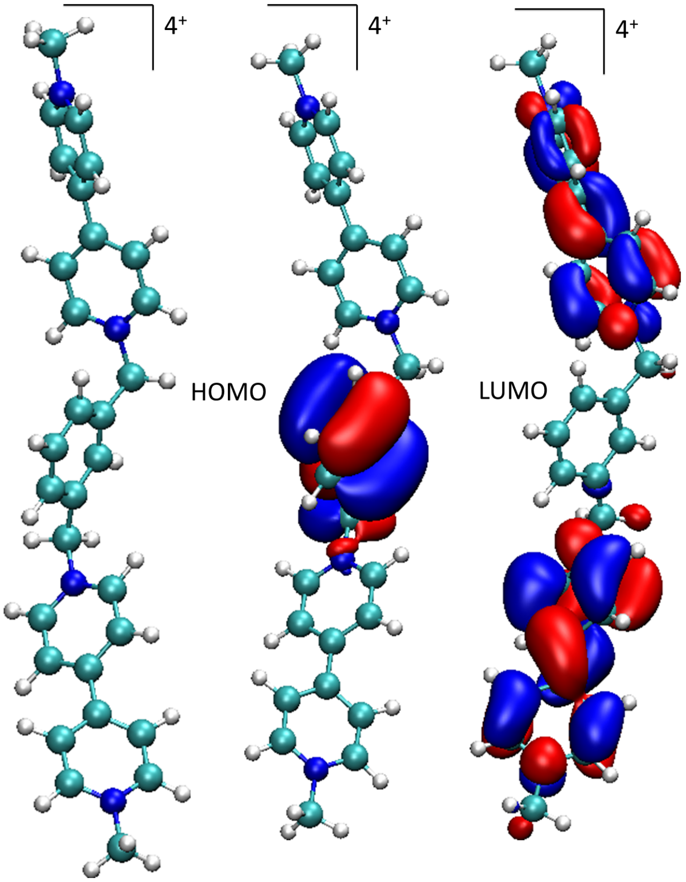

Figure S2. Viologen dimer (**2a**) at 4+ state of charge and optimal configurations of its HOMO and LUMO orbitals.

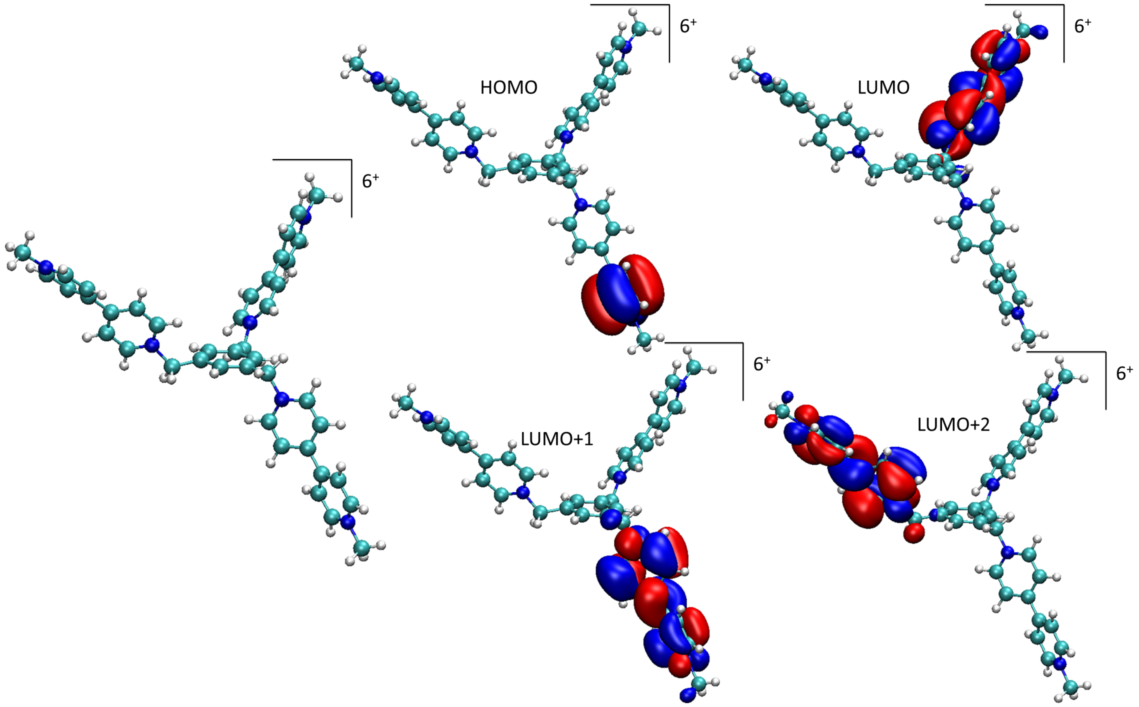

Figure S3. Viologen trimer (**3a**) at 6+ state of charge and optimal configurations of its HOMO and LUMO orbitals. LUMO, LUMO+1, and LUMO+2 are nearly degenerate.

The LUMO orbitals are well delocalized over the viologen branches in the highest and lower charge states (not shown). This implies that Coulombic repulsion between branches of viologen dimers and trimers maintains the open molecular structure. We also found no molecular orbital overlap between viologens and solvent (ACN) molecules or PF_6^- ions.

Table S1. Comparison between two charge schemes: GAFF *vs.* Mulliken charges from ab initio DFT calculations: **1a** at two different states of charge

GAFF		Mulliken		
1a^{1+}	**1a**$^{2+}$	**1a**$^{1+}$	**1a**$^{2+}$	
-0.086	-0.015	-0.085	-0.138	**C**
-0.216	-0.232	-0.167	-0.123	**C**
0.053	0.083	0.073	0.042	**C**
-0.206	-0.219	-0.167	-0.123	**C**
-0.115	-0.067	-0.085	-0.014	**C**
0.211	0.193	0.026	0.055	**N**
0.187	0.234	0.174	0.229	**H**
0.121	0.233	0.161	0.203	**H**
0.124	0.231	0.161	0.203	**H**
0.188	0.237	0.174	0.229	**H**
-0.141	-0.118	-0.026	-0.016	**C**
-0.205	-0.2	-0.208	-0.125	**C**
0.048	0.049	0.065	0.023	**C**
-0.177	-0.177	-0.208	-0.125	**C**
-0.188	-0.175	-0.026	-0.016	**C**
0.305	0.296	0.091	0.055	**N**
0.2	0.234	0.145	0.232	**H**
0.129	0.217	0.166	0.198	**H**
0.129	0.219	0.166	0.198	**H**
0.193	0.277	0.145	0.232	**H**
-0.29	-0.256	-0.124	0.0546	**C**
0.228	0.275	0.114	0.112	**H**
0.139	0.182	0.114	0.112	**H**
0.0085	-0.095	0.0222	-0.2	**C**
-0.097	-0.094	-0.074	-0.101	**C**
-0.152	-0.138	-0.129	-0.119	**C**
-0.125	-0.132	-0.148	-0.069	**C**
-0.136	-0.134	-0.129	-0.119	**C**
-0.133	-0.11	-0.074	-0.101	**C**
0.134	0.145	0.161	0.141	**H**
0.173	0.204	-0.128	0.166	**H**
0.174	0.201	0.555	0.169	**H**
0.174	0.193	-0.128	0.166	**H**
0.131	0.144	0.161	0.141	**H**
-0.347	-0.352	0.0089	-0.042	**C**
0.218	0.232	0.074	0.116	**H**
0.186	0.252	0.074	0.116	**H**
0.161	0.181	0.744	0.116	**H**

Table S2. Comparison between two charge schemes: GAFF *vs.* Mulliken charges from ab initio DFT calculations: acetonitrile and PF_6^-

Mulliken	GAFF	
ACN	**ACN**	
0.206	0.2087	**C**
-0.438	-0.376	**N**
-0.29	-0.05	**C**
0.1734	0.0707	**H**
0.1734	0.0707	**H**
0.1734	0.0707	**H**
PF_6 (1-)	**PF_6 (1-)**	
0.6483	1.2416	**P**
-0.275	-0.374	**F**
-0.275	-0.374	**F**
-0.275	-0.374	**F**
-0.275	-0.374	**F**
-0.275	-0.374	**F**
-0.275	-0.374	**F**

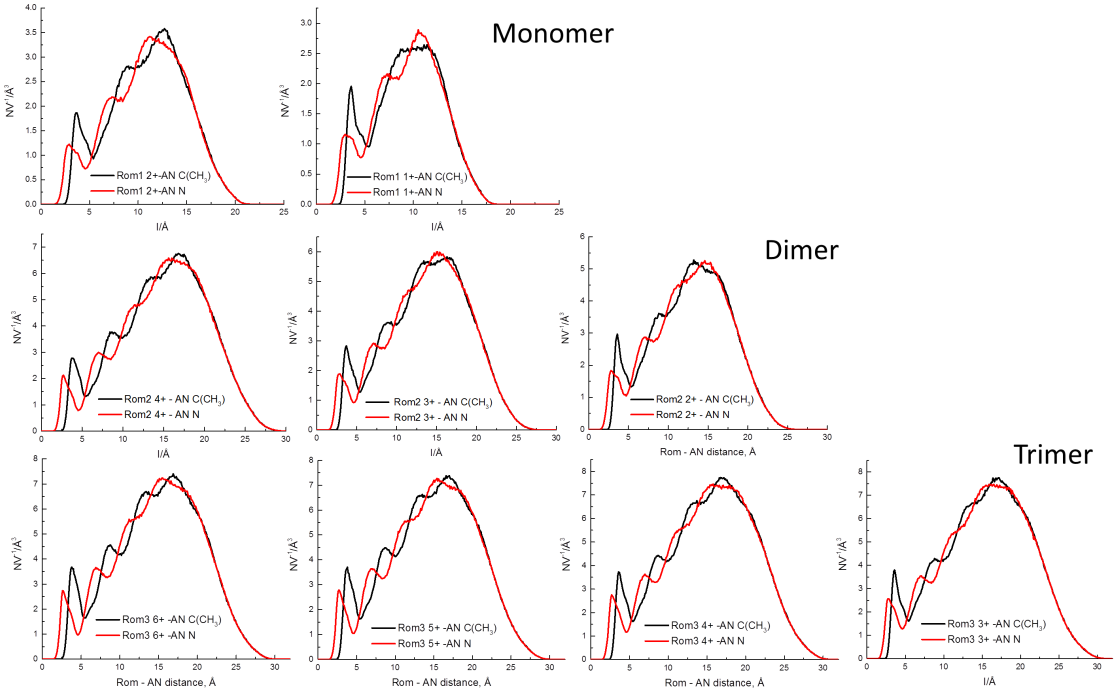

Figure S4. Acetonitrile preferentially orients with its electron-rich nitrile group towards the cationic monomer (**1a**, top row), dimer (**2a**, second row), and trimer (**3a**, third row). The black traces correspond to the RAO–ACN($\mathit{C}\mathrm{H}_3$) spacing, while red traces correspond to the RAO–ACN($\mathrm{C}\mathit{N}$) spacing.

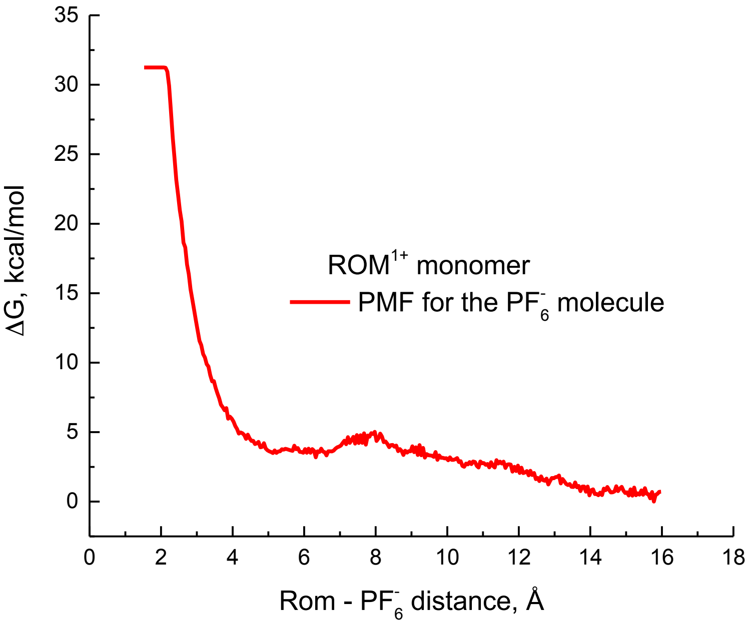

Figure S5. Free energy profile for **1a**$^{1+}$. The collective variable is the distance between centers of masses of ROM and PF_6^-. C_{ROM}=0.1 M

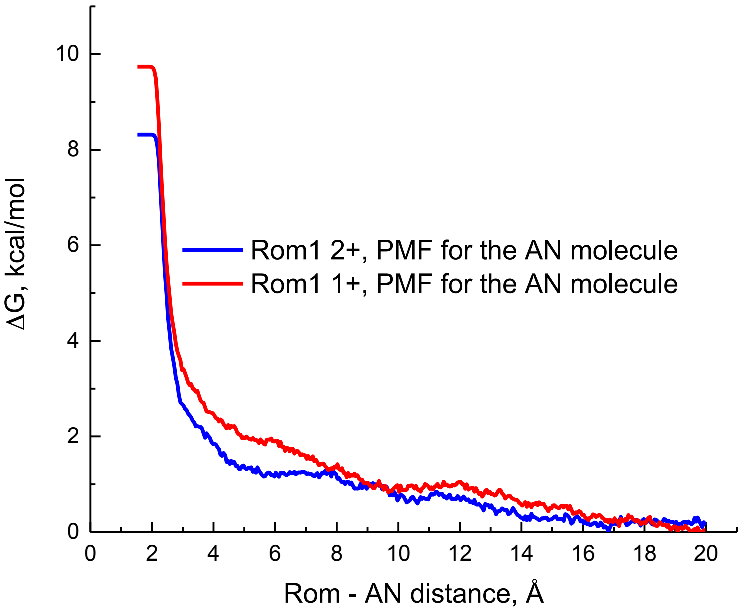

Figure S6. Free energy profiles for **1a**$^{1+}$ and **1a**$^{2+}$. The collective variable is the distance between centers of mass of ROM and ACN. C_{ROM}=0.1 M

Electrochemical properties of ROM and RAOs

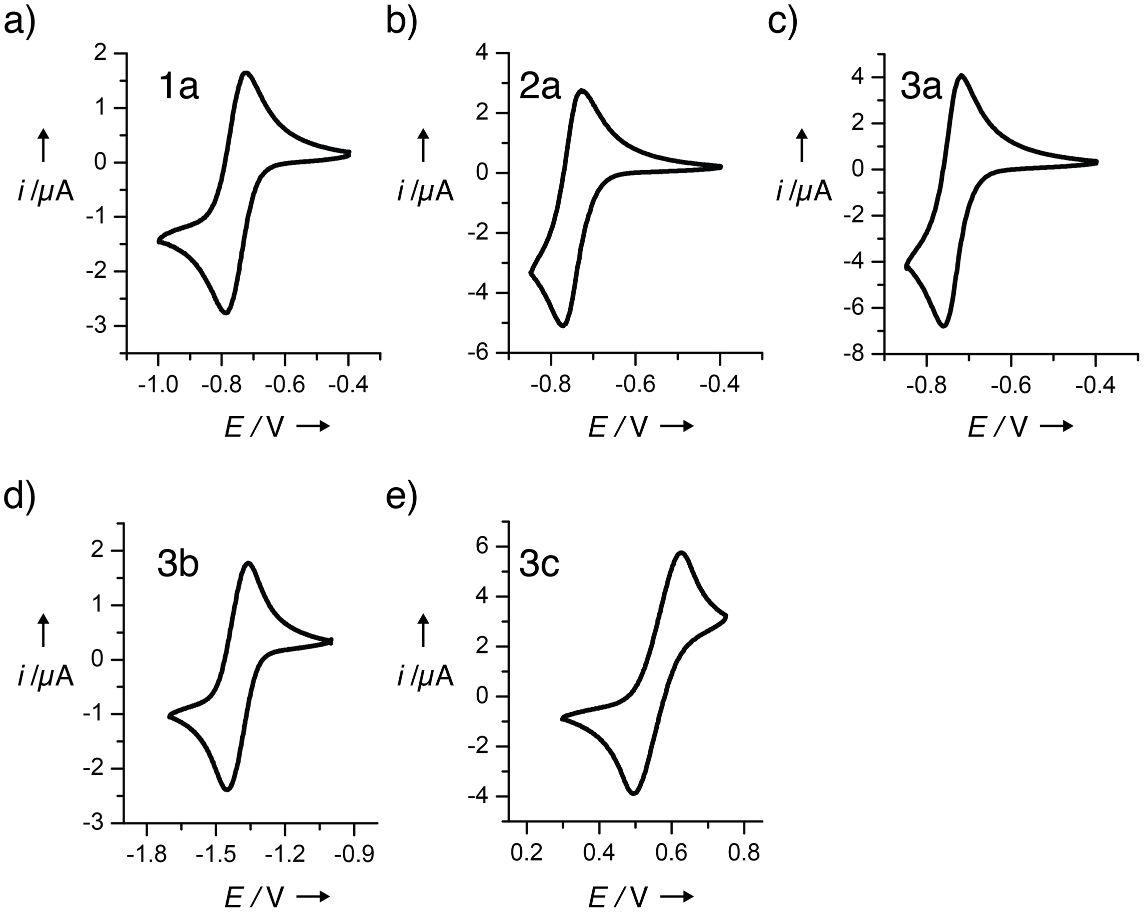

Figure S7. Cyclic voltammetry of a) **1a**, b) **2a**, c) **3a**, d) **3b**, and e) **3c**. All cyclic voltammograms were collected with a 1 mm glassy carbon working electrode and Pt wire counter-electrode. All potentials are given *vs.* Ag/Ag^+. The scan rate was 100 mV s^{-1}. All CVs were acquired with 1 mM ROM in 0.1 M $LiPF_6$ in acetonitrile (a–c), 0.1 M $TBAPF_6$ in propylene carbonate (d), or 0.1 M $TBAPF_6$ in dimethoxyethane (e).

Table S3. Redox potentials of ROM and RAOs **1a**–**3c** calculated from CVs acquired with: C_{ROM}=1 mM and v =100 mV s^{-1}

Molecule	Electrolyte	$E_{1/2}$ (V *vs.* Ag/Ag$^+$)	ΔE_p (mV)
Viologen monomer (**1a**)	0.1 M $LiPF_6$ in ACN	–0.756	58
Viologen dimer (**2a**)	0.1 M $LiPF_6$ in ACN	–0.752	38
Viologen trimer (**3a**)	0.1 M $LiPF_6$ in ACN	–0.742	39
Acylpyridinium trimer (**3b**)	0.1 M $TBAPF_6$ in PC	–1.404	88
DB3 trimer (**3c**)	0.1 M $TBAPF_6$ in DME	0.562	124

Crossover measurements and analysis

A membrane of known thickness (typically 10–25 µm) was placed between two halves of an H-cell with an aperture diameter of 1.6 cm and sealed in place with a chemically resistant O-ring. One half of the H-cell (the retentate) was charged with 10 mL of 0.100 M ROM monomer (**1a**), 0.050 M dimer (**2a**), or 0.033 M trimer (**3a**, **3b**, or **3c**) in electrolyte, while the other half (the permeate) was charged with the same volume of electrolyte with no ROM (or RAO). For viologen-based ROM and RAOs (**1a**–**3a**), the salt concentration in the permeate was increased to 0.250, 0.225, and 0.215 M for the monomer, dimer, and trimer experiments, respectively, in order to minimize the initial osmotic pressure difference between the two compartments. Similarly, for acylpyridinium trimer **3b**, the salt concentration in the permeate was increased to 0.166 M. Both compartments were stirred to ensure homogeneity. Every 5–60 min, the stirring was stopped and the concentration of ROM or RAO in the permeate was measured electrochemically by acquiring a CV at 100 mV s^{-1} from –0.40 to –0.85 V (for **1a**, **2a**, and **3a**), –1.00 to –1.70 V (for **3b**), or 0.30 to 0.75 V (for **3c**) *vs.* Ag/Ag$^+$. The peak cathodic (for **1a**, **2a**, **3a**, and **3b**) or anodic (for **3c**) current was related to ROM concentration with a calibration curve (Fig. S8 and Table S4). To test the effect of state-of-charge on crossover behavior, a 0.100 M solution of **1a** was reduced by bulk electrolysis to –0.65 V *vs.* Ag/Ag$^+$ and the crossover behavior of the resulting solution was measured in the same way as non-reduced **1a**.

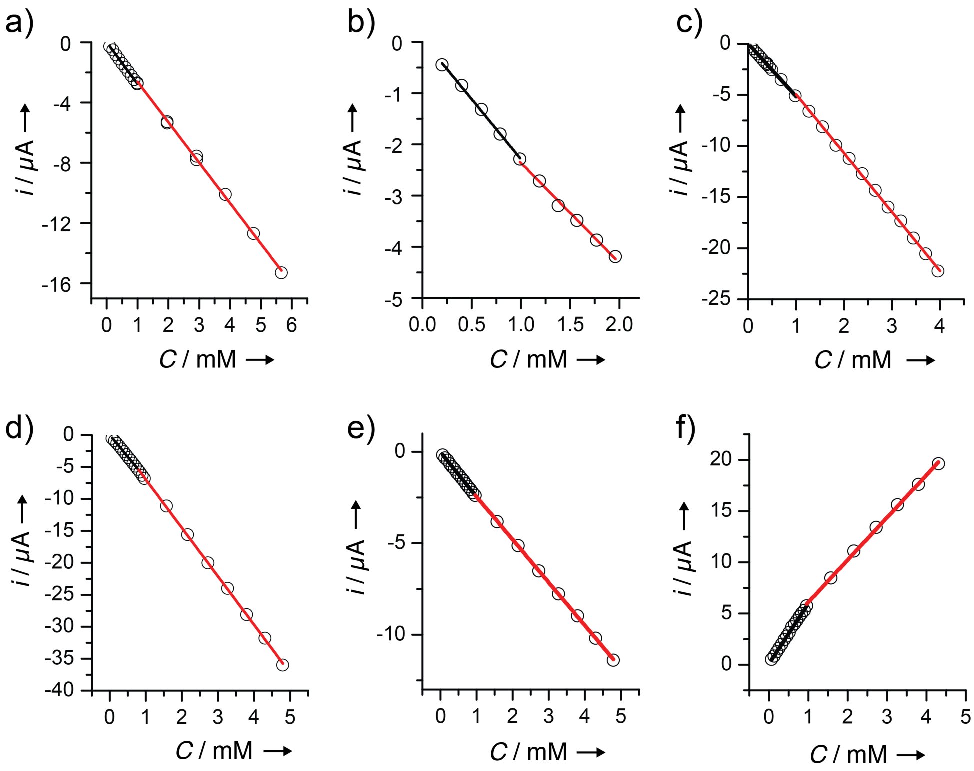

Figure S8. Calibration plots for a) viologen monomer (**1a**), b) reduced viologen monomer (**1a**), c) viologen dimer (**2a**), d) viologen trimer (**3a**), e) acylpyridinium trimer (**3b**), and f) DB3 trimer (**3c**). The black and red lines correspond to the low and high concentration calibration regimes, respectively.

Table S4. Calibration curve parameters and fitting errors for each ROM and RAO

Molecule	Slope (mA/mM)	Intercept (mM)	R^2
Viologen-based ROM and RAOs			
1a (low conc.)	$(-2.77 \pm 0.02) \times 10^{-3}$	$(0 \pm 2) \times 10^{-5}$	0.9993
1a (high conc.)	$(-2.69 \pm 0.05) \times 10^{-3}$	$(0 \pm 2) \times 10^{-4}$	0.9986
1a, reduced (low conc.)	$(-2.34 \pm 0.05) \times 10^{-3}$	$(5 \pm 3) \times 10^{-5}$	0.9987
1a, reduced (high conc.)	$(-1.95 \pm 0.07) \times 10^{-3}$	$(-4 \pm 1) \times 10^{-4}$	0.9943
2a (low conc.)	$(-5.18 \pm 0.04) \times 10^{-3}$	$(2 \pm 2) \times 10^{-5}$	0.9992
2a (high conc.)	$(-5.76 \pm 0.05) \times 10^{-3}$	$(8 \pm 2) \times 10^{-4}$	0.9992
3a (low conc.)	$(-6.85 \pm 0.06) \times 10^{-3}$	$(2 \pm 3) \times 10^{-5}$	0.9993
3a (high conc.)	$(-7.57 \pm 0.04) \times 10^{-3}$	$(6 \pm 1) \times 10^{-4}$	0.9998
Acylpyridinium-based RAOs			
3b (low conc.)	$(-2.46 \pm 0.02) \times 10^{-3}$	$(-1 \pm 1) \times 10^{-5}$	0.9994
3b (high conc.)	$(-2.34 \pm 0.01) \times 10^{-3}$	$(-11 \pm 3) \times 10^{-5}$	0.9999
DB3-based RAOs			
3c (low conc.)	$(5.89 \pm 0.06) \times 10^{-3}$	$(10 \pm 3) \times 10^{-5}$	0.9988
3c (high conc.)	$(4.14 \pm 0.05) \times 10^{-3}$	$(20 \pm 2) \times 10^{-4}$	0.9991

Calculation of *D*D_{eff} from crossover measurements

At any moment, the flux of active-species across the membrane (*J*, mol cm^{-2} s^{-1} can be described with Fick's first law:

$$J = D_{eff}\frac{\partial C}{\partial x} = D_{eff}\frac{C_{retentate}(t) - C_{permeate}(t)}{l}$$

Where *C* is the concentration in mol cm^{-3} and *l* is the membrane thickness in cm. For short times, the difference $C_{retentate}(t) - C_{permeate}(t)$ does not change significantly from its initial value of $C_{retentate}(t_0) - C_{permeate}(t_0) = C_0$, and the flux is constant with time:

$$J_{t\sim 0} = D_{eff}\frac{C_0}{l}$$

The concentration of active species in the permeate compartment can be calculated by integrating the flux of active species and dividing by the volume of solution in the permeate compartment:

$$C_{permeate}(t) = \frac{A\int_0^t J(t)dt}{V_{permeate}} = \frac{D_{eff}C_0A}{lV_{permeate}}t$$

By measuring active-species concentration in the permeate compartment and plotting these values as a function of time, the effective diffusion coefficient of the active-species through the membrane can be quantified.

Limit of quantification

As the salt concentration between the retentate and permeate equalizes, an osmotic pressure difference builds between the two compartments. This induces osmotic flow of solvent from the permeate into the retentate, thus rendering measurements after this time invalid due to competing convection and diffusion in opposite directions. In acetonitrile, this solvent movement was never observed for times < 36 hours, so the lower limit of quantification for D_{eff} is set by this time and the minimum quantifiable ROM concentration. In propylene carbonate, this solvent movement wasn't observed even after 1 week, so the lower limit of quantification for D_{eff} is set by the duration of the experiment.

Summary of crossover measurements

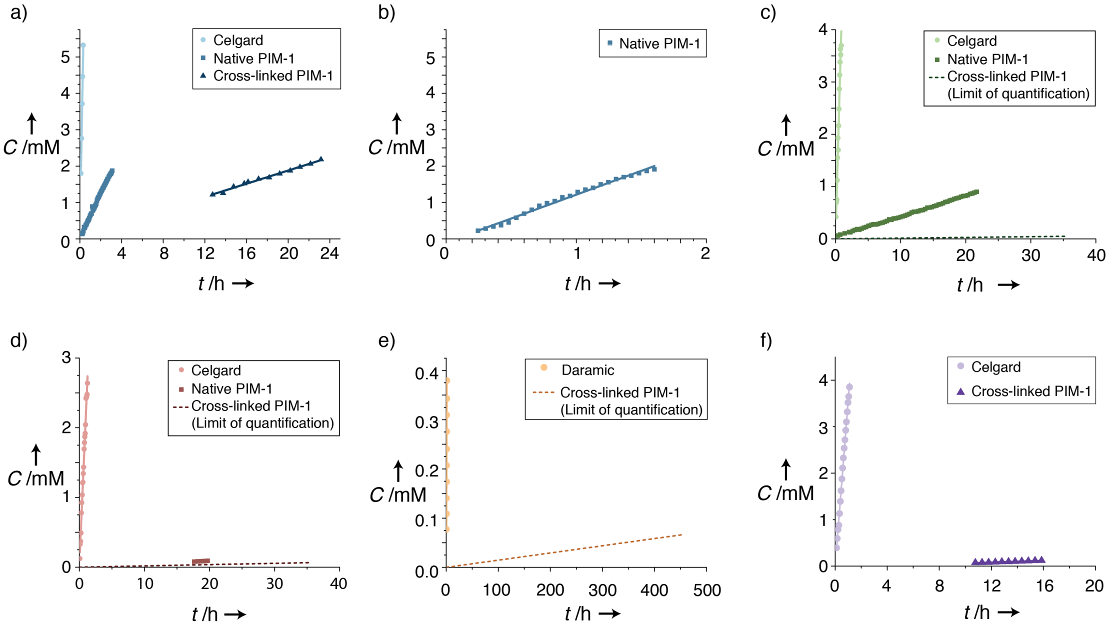

Figure S9. Measured concentration of ROM or RAO in the permeate compartment as a function of time (points) and linear fits (lines) for a) viologen monomer (**1a**), b) reduced viologen monomer (**1a**), c) viologen dimer (**2a**), d) viologen trimer (**3a**), e) acylpyridinium trimer (**3b**), and f) DB3 trimer (**3c**). Circles represent Celgard (or Daramic for panel e), squares represent native PIM-1, and triangles represent cross-linked PIM-1 membranes. The dashed lines in panels c–e represent the maximum possible crossover rate for each molecule through cross-linked PIM-1 membranes, as none of these experiments surpassed the limit of quantification during the tested time.

Table S5. Measured values for D_{eff} (in cm^2 s^{-1}) for all membrane/RAO pairings. * indicates that D_{eff} was below the limit of quantification, so the reported value is an upper-bound for D_{eff}. † indicates that the measurement was performed with Daramic instead of Celgard due to poor wetting of Celgard with propylene carbonate.

	Celgard	**Native PIM-1**	**Cross-linked PIM-1**
Viologen-based ROM and RAOs			
Monomer (1a)	$(5.4 \pm 0.4) \times 10^{-7}$	$(1.3 \pm 0.1) \times 10^{-8}$	$(1.1 \pm 0.1) \times 10^{-9}$
Monomer, reduced (1a)	–	$(2.2 \pm 0.2) \times 10^{-8}$	–
Dimer (2a)	$(3.1 \pm 0.3) \times 10^{-7}$	$(9 \pm 1) \times 10^{-10}$	3.4×10^{-11} *
Trimer (3a)	$(2.2 \pm 0.2) \times 10^{-7}$	$(2.1 \pm 0.3) \times 10^{-10}$	8.4×10^{-11} *
Acylpyridinium-based RAOs			
Trimer (3b)	$(2.6 \pm 0.2) \times 10^{-7}$ †	–	1.0×10^{-11} *
DB3-based RAOs			
Trimer (3c)	$(3.7 \pm 0.3) \times 10^{-7}$	–	$(8.1 \pm 0.7) \times 10^{-10}$

Calculation of D_{sol} for viologen ROM and ROAs 1a–3a

The size and shape of viologen monomer (**1a**), dimer (**2a**), and trimer (**3a**) can be described by the smallest oblate spheroid that encompasses all of the atoms in each relaxed chemical structure. The predicted diffusion coefficient (D_{sol}) of these spheroids can be calculated using a modified form of the Stokes-Einstein equation[15] that takes into account the non-spherical shape of these molecules, as well as the ratio between solute and solvent size:

$$D_{sol} = \frac{kT}{c(r_{solv}, r_H) f_s(a,b) \pi \eta r_H}$$

where D_{sol} is the molecule's diffusion coefficient in solution in $m^2\ s^{-1}$, k is the Boltzmann constant, T is the temperature in K, $c(r_{solv}, r_H)$ is a correction factor for molecules that are similar in size to the solvent,[16] $f_s(a,b)$ is a correction factor for non-spherical molecules,[17] η is the solvent's viscosity in Poise, and r_H is the molecule's hydrodynamic radius in m. For large, spherical molecules, the product $cf_s = 6$, yielding the Stokes-Einstein equation.

Table S6. Dimensions and volume of the oblate spheroids that encompass the calculated structures of **1a**, **2a**, and **3a**, along with the calculated Stokes-Einstein (assuming spherical shape and small solvent size) and modified Stokes-Einstein (using the known shape and solvent size) diffusion coefficients in acetonitrile.

Species	***a* axis (Å)**	***c* axis (Å)**	**Volume (Å^3)**	**Stokes-Einstein D_{sol} (cm^2 s^{-1})**	**Modified Stokes-Einstein D_{sol} (cm^2 s^{-1})**
Monomer (**1a**)	3.75	6.00	353.4	1.5×10^{-5}	1.6×10^{-5}
Dimer (**2a**)	4.38	12.25	984.4	1.0×10^{-5}	1.0×10^{-5}
Trimer (**3a**)	12.25	3.94	2476.6	7.6×10^{-6}	7.1×10^{-6}

Characterization of cross-linked PIM-1 membranes

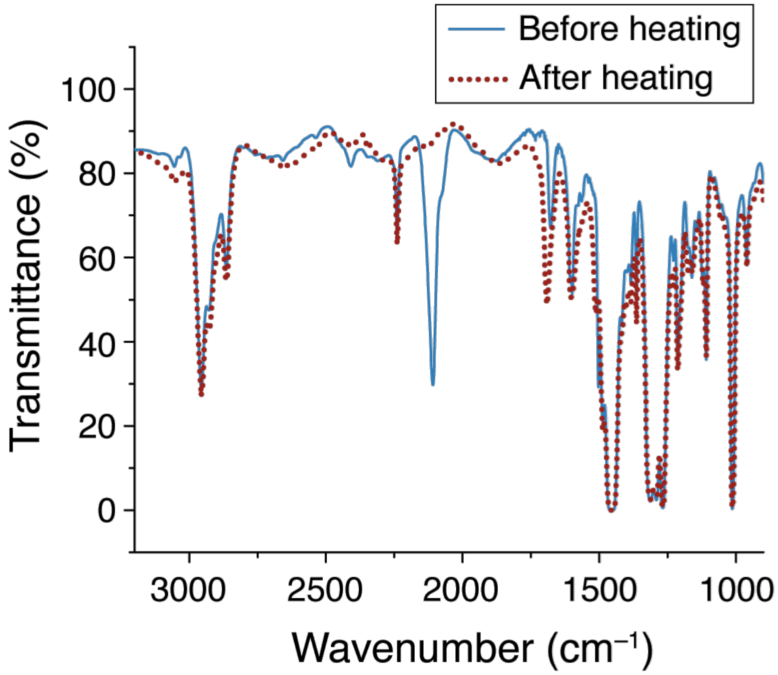

Figure S10. FT-IR spectra of membranes cast from PIM-1 with 0.1 molar equivalents of cross-linker before (blue, solid) and after (red, dotted) heating at 175 ˚C for 7.5 h. Complete disappearance of the azide peak at 2110 cm^{-1} indicates complete reaction of the cross-linker.

Membrane ionic conductivity

Membranes with a diameter of 14 mm were soaked in electrolyte and sandwiched between two 12 mm diameter stainless steel electrodes in a Swagelok cell, with the excess membrane folded around one of the electrodes. Electrochemical impedance spectra were acquired on a Biologic VMP3 at a 0 V DC bias and 10 mV AC bias from 200 kHz to 1 kHz. The data were fitted to an equivalent circuit (Fig. S11) with the EC-Lab software by minimizing the fitting error, χ^2 given by $\chi^2 = \sum_i \frac{\left(Z_{meas}(f_i) - Z_{fit}(f_i)\right)^2}{|Z_{meas}(f_i)|}$. The equivalent circuit accounts for the resistance and inductance of the wiring connecting the potentiostat and the conductivity cell, which were measured to be 0.34 Ω and 2.7×10^{-6} H, respectively. All capacitors were modeled as constant phase elements, which have an impedance given by $Z(f) = [Q(j2\pi f)^{\alpha}]^{-1}$. When α is 0, the CPE acts as a perfect resistor, and when α is 1, it acts as a perfect capacitor. For intermediate values of α, the CPE acts as a "leaky capacitor." The membrane conductivity was calculated from the membrane resistance using the relation $\sigma = l(AR_M)^{-1}$, where σ is the membrane conductivity in S cm^{-1}, l is the membrane thickness in cm, A is the electrode area in cm^2, and R_M is the membrane resistance in Ω.

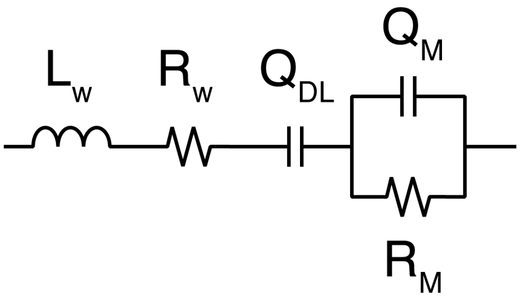

Figure S11. Equivalent circuit used to model electrochemical impedance spectra of membranes soaked in electrolyte. R_W and L_W correspond to the resistance and inductance of the wiring leading from the potentiostat to the conductivity cell, respectively. Q_{DL} and Q_M correspond to the double layer and membrane capacitances, and R_M corresponds to the ionic resistance of the membrane.

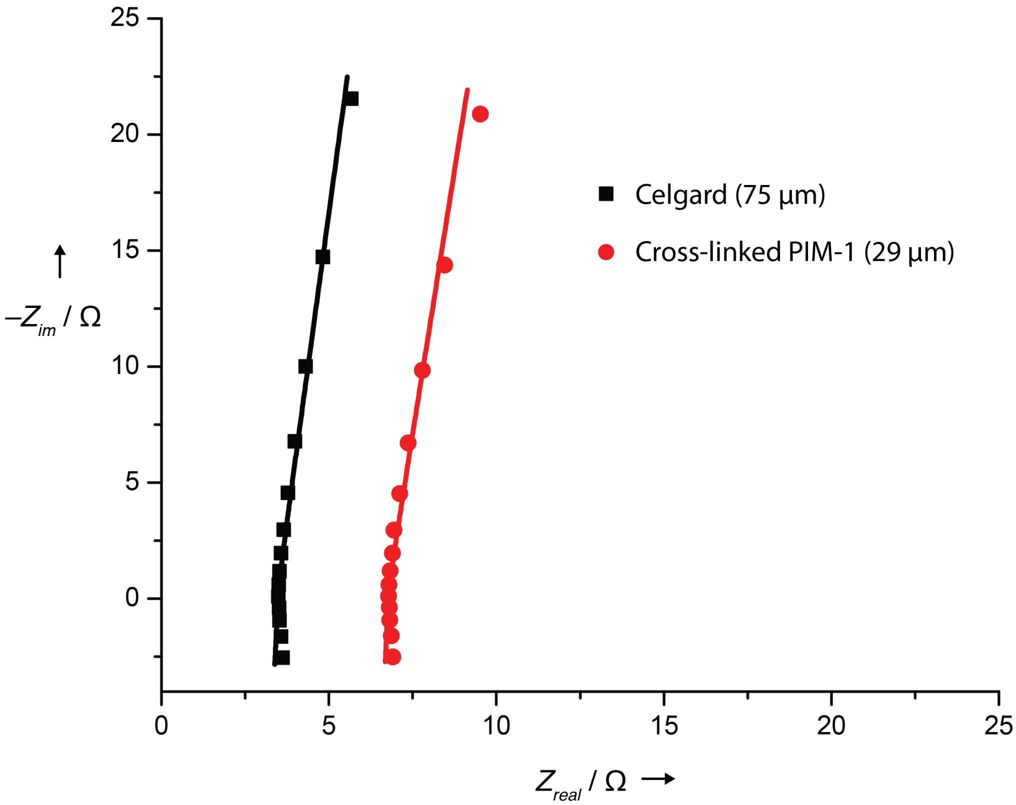

Figure S12. Measured EIS spectra (points) for Celgard (black squares) and cross-linked PIM-1 (red circles) membranes along with fits (lines)

Table S6. Fitting parameters for EIS spectra

Membrane	**Membrane Thickness (µm)**	Q_{DL} **(Fs$^{\alpha-1}$) [α]**	Q_M **(Fs$^{\alpha-1}$) [α]**	R_M **(Ω)**	**σ (mS cm^{-1})**
Celgard (3×)	75	11.9×10^{-6} [0.94]	35.5×10^{-9} [1.00]	3.086	2.15
Cross-linked PIM-1 (3×)	29	13.3×10^{-6} [0.93]	10.5×10^{-9} [1.00]	6.371	0.40

References

[1] G. Nagarjuna, J. Hui, K. J. Cheng, T. Lichtenstein, M. Shen, J. S. Moore, J. Rodríguez-López, *J. Am. Chem. Soc.* **2014,** *136*, 16309.

[2] P. M. Budd, E. S. Elabas, B. S. Ghanem, S. Makhseed, N. B. McKeown, K. J. Msayib, C. E. Tattershall, D. Wang, *Adv. Mater.* **2004,** *16*, 456.

[3] C. Li, A. L. Ward, S. E. Doris, T. A. Pascal, D. Prendergast, B. A. Helms, *Nano Lett.* **2015,** *15*, 5724.

[4] S. E. Doris, A. L. Ward, P. D. Frischmann, L. Li, B. A. Helms, *J. Mater. Chem. A* **2016,** *4*, 16946.

[5] J. Wang, R. M. Wolf, J. W. Caldwell, P. A. Kollman, D. A. Case, *J. Comput. Chem.* **2004,** *25*, 1157.

[6] A. Laio, M. Parinello, *Proc. Natl. Acad. Sci.* **2002,** *99*, 12562.

[7] G. Bussi, A. Laio, M. Parinello, *Phys. Rev. Lett.* **2006,** *96*, 090601.

[8] I. S. Ufimtsev, T. J. Martinez, *J. Chem. Theory Comput.* **2009,** *5*, 2619.

[9] S. Zahn, D. R. MacFarlane, E. I. Izgorodina, *Phys. Chem. Chem. Phys.* **2013,** *15*, 13664.

[10] S. Grimme, J. Antony, S. Ehrlich, H. Krieg, *J. Chem. Phys.* **2010,** *132*, 154104.

[11] J. Kästner, J. M. Carr, T. W. Keal, W. Thiel, A. Wander, P. Sherwood, *J. Phys. Chem. A* **2009,** *113*, 11856.

[12] S. Plimpton, *J. Comp. Phys.* **1995,** *117*, 1.

[13] S. A. Nosé, *J. Chem. Phys.* **1984,** *81*, 511.

[14] W. G. Hoover, *Phys. Rev. A: At. Mol. Opt. Phys.* **1985,** *31*, 1965.

[15] A. Macchioni, G. Ciancaleoni, C. Zuccaccia, D. Zuccaccia, *Chem. Soc. Rev.* **2008,** *37*, 479.

[16] H.-C. Chen, S.-H. Chen, *J. Phys. Chem.* **1984,** *88*, 5118.

[17] F. Perrin, *J. Phys. Radium* **1936,** *7*, 1.